

Supporting Information

for *Adv. Optical Mater.*, DOI: 10.1002/adom.202200354

Silver-Bismuth Based 2D Double Perovskites
(4FPEA)₄AgBiX₈ (X = Cl, Br, I): Highly Oriented Thin
Films with Large Domain Sizes and Ultrafast Charge-
Carrier Localization

*Rik Hooijer, Andreas Weis, Alexander Biewald,
Maximilian T. Sirtl, Julian Malburg, Rico Holfeuer, Simon
Thamm, Amir Abbas Yousefi Amin, Marcello Righetto,
Achim Hartschuh, Laura M. Herz, and Thomas Bein**

Supporting Information

Silver-Bismuth based 2D Double Perovskites (4FPEA)₄AgBiX₈ (X=Cl, Br, I): Highly Oriented Thin Films with Large Domain Sizes and Ultrafast Charge-Carrier Localization

*Rik Hooijer, Andreas Weis, Alexander Biewald, Maximilian T. Sirtl, Julian Malburg, Rico Holfeuer, Simon Thamm, Amir Abbas Yousefi Amin, Marcello Righetto, Achim Hartschuh, Laura M. Herz, Thomas Bein**

S1

Our attempts to synthesize (PEA)₄AgBiI₈, (2FPEA)₄AgBiI₈ and (3FPEA)₄AgBiI₈ in the same way as for (4FPEA)₄AgBiI₈ yielded only hybrid bismuth iodides. The resulting crystalline powder is of orange color compared to the red colored (4FPEA)₄AgBiI₈ and the resulting diffractogram differs greatly from the expected diffractogram that should be close to the standard $n = 1$ double perovskite patterns, this is shown in Figure S1. Furthermore, we performed EDX measurements on said powder and confirm the absence of any Ag, only showing the presence of Bi and I as seen in Table S1.

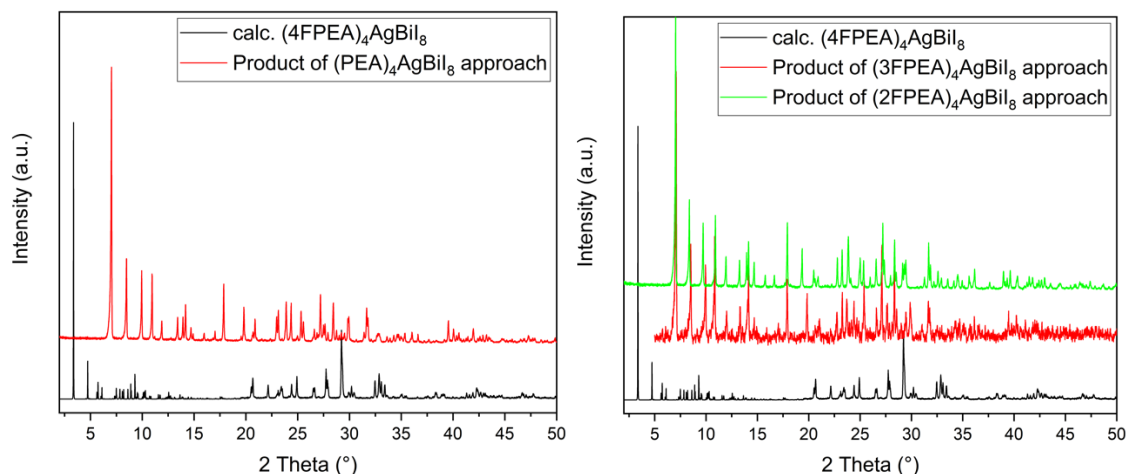


Figure S1: Diffractogram of the products of the synthesis approaches for a) (PEA)₄AgBiI₈ and (2FPEA)₄AgBiI₈ compared to the calculated diffractogram of (4FPEA)₄AgBiI₈.

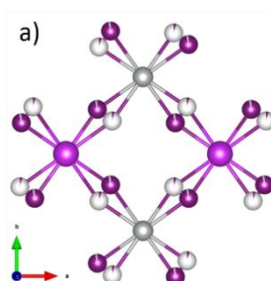
Table S1: EDX data for the crystalline products of the synthesis approach for $(\text{PEA})_4\text{AgBiI}_8$.

Measurement	Ag (at%)	Bi (at%)	I (at%)	Ratio (Bi:I)
1	-	13.51	86.49	1:6.40
2	-	12.23	87.77	1:7.18
3	-	13.66	86.32	1:6.32
4	-	15.36	84.64	1:5.51
5	-	15.05	84.95	1:5.65
6	-	15.26	84.74	1:5.55

S2

The structure of $(4\text{FPEA})_4\text{AgBiI}_8$ has been refined as a 2-component pseudomerohedral twin (pseudo-monoclinic cell). The twin volume ratio of the two domains refined to 0.75/0.25.

Two iodides are slightly disordered, the ratio of site occupation factors refined to 0.97/0.03.

**Figure S2:** Iodide Disorder in the single crystal structure of $(4\text{FPEA})_4\text{AgBiI}_8$.**S3 and S4**

The structures $(4\text{FPEA})_4\text{AgBiBr}_8$ and $(\text{PEA})_4\text{AgBiBr}_8$ display different levels of organic interlayer stacking effects. We note that the structures of $(4\text{FPEA})_4\text{AgBiBr}_8$ and $(4\text{FPEA})_4\text{AgBiI}_8$ are sufficiently similar (as seen in Figure 1) to explain why $(\text{PEA})_4\text{AgBiI}_8$ cannot be obtained without additional control of the interactions between layers. By simple comparison of the organic layers in the four shown directions (Figure S4), the increased order of the 4FPEA^+ cations vs. the PEA^+ cations can be observed. When viewed along a , the ring-to-ring stacking for both seems similar, but when viewed along b the twisting of the PEA^+ moiety can be seen distinctly. In Figure S4 this is visualized by red lines connecting equal carbon atom positions in 4FPEA^+ and PEA^+ and a yellow dot/lines displaying the channel formed by the arranged phenyl rings. The aromatic rings of 4FPEA^+ are stacked in-plane of the organic layer along ab as well as out-of-plane along c , while PEA^+ is only stacked in-plane of the organic layer along ab and not also out-of-plane along c , which is a reason for the stabilizing binding effect between the organic layers. Furthermore, while in-plane stacking of 4FPEA^+ cations is present in only one direction, as seen when viewed along b (Figure S4 b)),

PEA⁺ cations in-plane stacking is present in two directions in an alternating fashion (Figure S4 b) and d)). This increased out-of-plane stacking effect of the 4FPEA⁺ moieties could be caused by the increased dipole moment of the molecule and/or the fluorine-fluorine attraction, leading to the observed point-symmetric anti stacking of the phenyl-rings (Figure S4 b) and d)).^[1, 2] The calculated dipole moment for PEA⁺ is 13.47 Debye, whereas for 4FPEA⁺ the value increases to 17.50 Debye, visualized in Figure S5. We further note that the substitution position of the fluorine atom seems crucial for the stabilizing effect for the 2D hybrid double perovskite iodide. While for lead- and tin-based 2D hybrid perovskites the ortho, meta and para position of the fluorine all yield the desired $n = 1$ 2D hybrid double perovskite phase, our attempts with 2FPEA⁺ and 3FPEA⁺ only yielded hybrid bismuth iodides (Figure S1), confirming that not only sufficient binding effects but also specific geometric requirements of the organic cation are needed to stabilize the silver bismuth iodide system.^[3, 4] This is best seen in Figure S3, where the in-plane stacking of the phenyl rings is observable for both structures in b) and d), but the out of plane organic layer stacking is only seen in (4FPEA)₄AgBiBr₈ in a) compared to (PEA)₄AgBiBr₈ in c). This difference is displayed more in detail in Figure S4, where only the organic part of the structures is shown. Red dotted lines illustrate the stacking positions of layer-to-layer stacking of adjacent phenyl rings and yellow dotted lines illustrate the in-plane stacking of adjacent phenyl rings. It is apparent that the 4FPEA molecules are arranged orderly in- and out-of-plane, while the PEA molecules are only ordered in-plane. The in-plane stacking is further worse for the PEA molecules, as they stack in an alternating manner, best seen in Figure S4 b) and d).

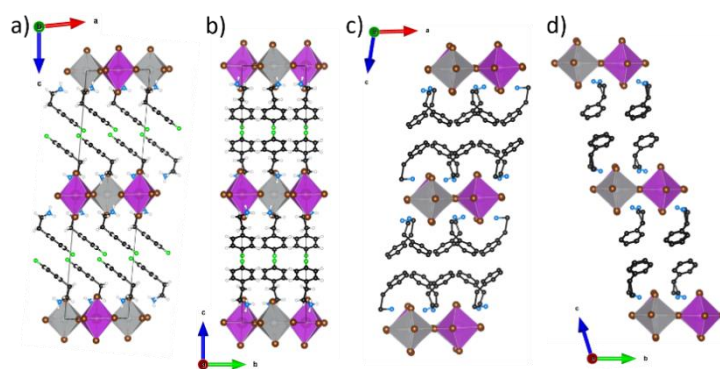


Figure S3: Comparison between the crystal structures of a) and b) (4FPEA)₄AgBiBr₈ and c) and d) (PEA)₄AgBiBr₈ along the b- and a-axis.

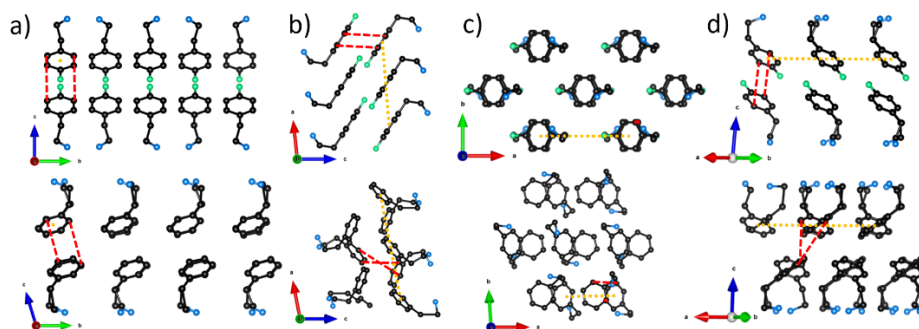


Figure S4: Comparison between the organic layers of (4FPEA)₄AgBiBr₈ on the top and (4FPEA)₄AgBiBr₈ on the bottom, along different crystallographic axis in a) b) c) and d).

S5

The dipole moment of the cations was calculated by using the Gaussian 16W suite, using DFT and the B3LYP functional in a 6-31G* basis set.^[5] The value for PEA⁺ is 13.4646 Debye, whereas for 4FPEA⁺ the value increased to 17.4947 Debye. The direction of the dipole moment is visualized in Figure S5 as a blue arrow, with the arrow head indicating the positive charged side and the arrow tail indicating the negative charged side. The difference in charge is visualized through an increased length of the arrow in 4FPEA. The increased dipole moment is one of the reasons for the increase in ordered stacking effect for 4FPEA vs PEA, alongside other effects like π - π stacking and fluorine-fluorine interactions.^[6]

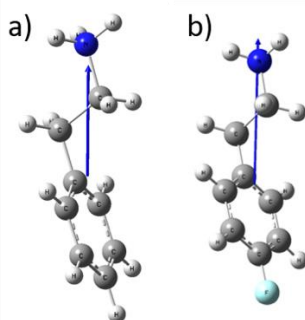


Figure S5: Dipole moments of a) PEA⁺ and b) 4FPEA⁺ visualized as blue arrows.

Table S2

The lattice parameters for (4FPEA)₄AgBiBr₈ and (4FPEA)₄AgBiI₈ were determined through the single crystal structure solution. For (4FPEA)₄AgBiCl₈ we performed indexing in EXPO 2014 using the indexing program N-TREOR09 and compared the given solutions with the two solved structures to choose the most plausible parameters.^[7] The lattice parameters are given in Table S2 and agree well with the powder patterns.

Table S2: Lattice parameters for $(4\text{FPEA})_4\text{AgBiX}_8$ ($X=\text{Cl, Br, I}$). Parameters for $(4\text{FPEA})_4\text{AgBiBr}_8$ and $(4\text{FPEA})_4\text{AgBiI}_8$ are obtained from the single crystal structure solution, while parameters for $(4\text{FPEA})_4\text{AgBiCl}_8$ were obtained from indexing powder XRD data.

Compound	a (Å)	b (Å)	c (Å)	α (°)	β (°)	γ (°)	V (Å ³)	Space Group
$(4\text{FPEA})_4\text{AgBiCl}_8$	8.1741	7.8068	16.7934	90	97.60	90	1062.2	P 1 21 1
$(4\text{FPEA})_4\text{AgBiBr}_8$	8.3833	8.1395	32.7693	90	96.120	90	2223.3	P 1 2/n 1
$(4\text{FPEA})_4\text{AgBiI}_8$	8.6236	8.7470	16.3676	98.973	90.119	90.013	1219.5	P-1

S6

Cross section of $(4\text{FPEA})_4\text{AgBiI}_8$ on SiO_2 showing a homogeneous coverage, with $(4\text{FPEA})_4\text{AgBiI}_8$ lightest contrast on top, 500 nm thick darker contrast SiO_2 below and a lighter contrast Si on the bottom.

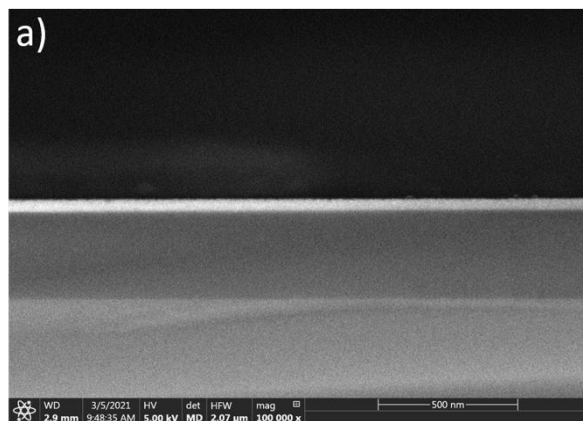


Figure S6: Cross section of $(4\text{FPEA})_4\text{AgBiI}_8$ on SiO_2 .

S7

To confirm the bulk powder products of $(4\text{FPEA})_4\text{AgBiBr}_8$ and $(4\text{FPEA})_4\text{AgBiI}_8$ we performed a profile refinement in EXPO 2014 employing a Pearson VII profile shape function, background modelling by a Chebyshev polynomial of degree 16 and a refinement of non-structural parameters with the LeBail method.^[7] The refinement values R_p and R_{wp} are in good agreement and the biggest deviations can be seen in the difference plots coming from the main reflex between $5-6^\circ 2\theta$, showing a large asymmetric peak shape which is caused by the small angle area and the resulting inaccuracy of the diffractometer. As there are no additional reflexes present in the difference plots or any reflexes missing we conclude the product to be phase pure.

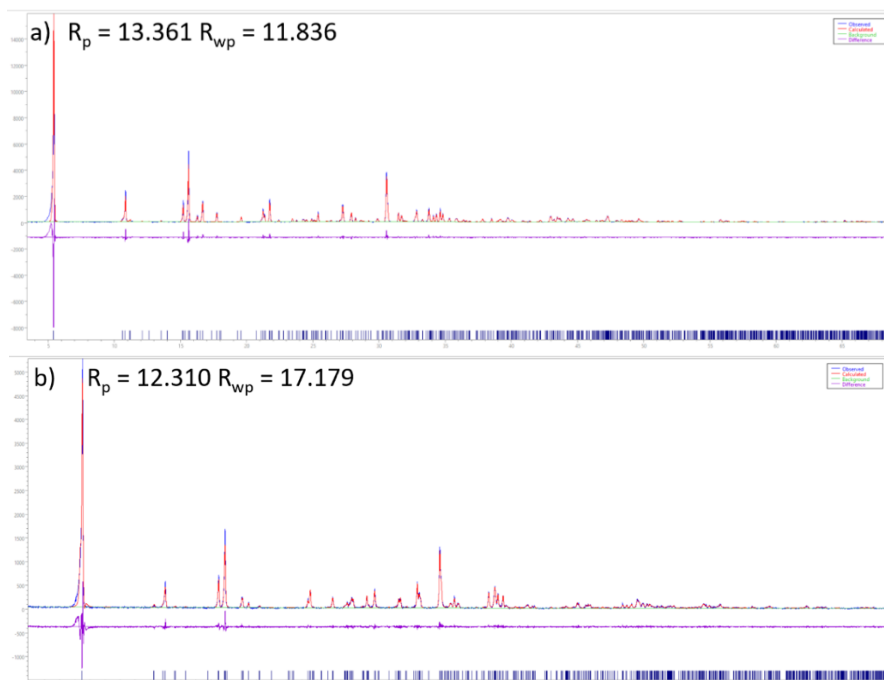


Figure S7: Profile Refinements for powder samples of a) $(4\text{FPEA})_4\text{AgBiBr}_8$ and b) $(4\text{FPEA})_4\text{AgBiI}_8$.

Table S3

To confirm the elemental composition and purity of the powder and thin films samples, we performed EDX measurements on crystalline powder samples and thin film samples shown in Table S3. Since the thin film samples on their respective substrates show an influence of the substrates on the measured signals causing an underestimation of the Ag, we scraped off the thin films from the substrates and measured them separately as powders. All samples agree well with the theoretic stoichiometry and the deviations are in the standard precision limits of the EDX method.

Table S3: EDX data for all $(4\text{FPEA})_4\text{AgBiX}_8$ (X=Cl, Br, I) in atom% from crystalline samples, thin film samples on ITO substrates and the same thin film samples scraped off and measured in powder form.

Sample	Ag (at%)	Bi (at%)	Cl (at%)	Ratio (Ag:Bi:X)
Crystal (avg.)	11.94	11.81	76.25	1.01:1:6.46
Thin Film (avg.)	5.86	10.24	83.90	0.57:1:8.19
Powdered Film (avg.)	9.69	12.00	78.32	0.81:1:6.53
	Ag (at%)	Bi (at%)	Br (at%)	
Crystal (avg.)	11.46	10.69	77.84	1.07:1:7.28
Thin Film (avg.)	5.73	9.02	85.26	0.63:1:9.45
Powdered Film (avg.)	12.43	11.14	76.42	1.12:1:6.86
	Ag (at%)	Bi (at%)	I (at%)	
Crystal (avg.)	10.59	10.02	79.40	1.06:1:7.92
Thin Film (avg.)	5.83	9.58	84.58	0.61:1:8.83
Powdered Film (avg.)	11.73	10.14	78.13	1.16:1:7.71

S8

AFM images of the substrates show the difference in surface roughness of a) Si-SiO₂ wafer, b) ITO coated-glass and c) FTO-coated glass, which is plotted in Figure S8 d) as a line cut across the full length of the substrate. The y-axis zero point was chosen to represent the average height value from the AFM measurement.

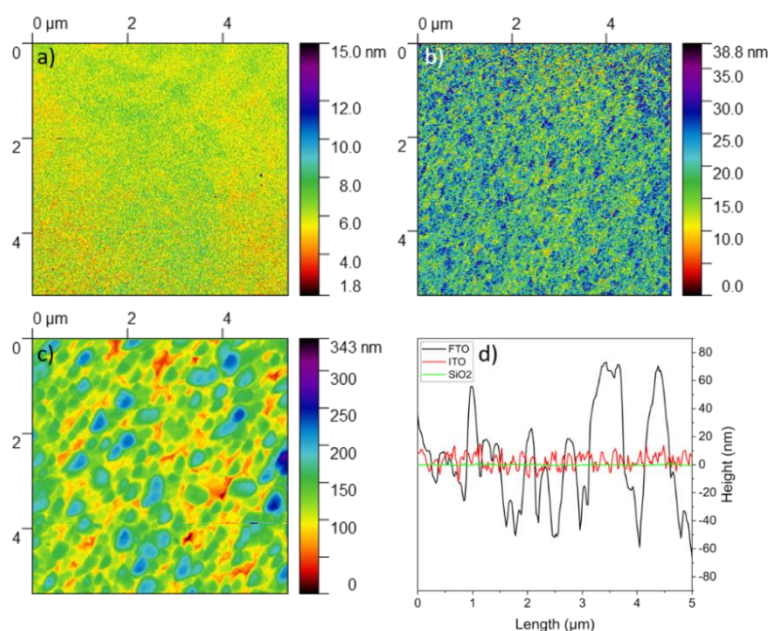


Figure S8: AFM images of substrates a) SiO₂, b) ITO, c) FTO and a line cut of each sample in d).

S9

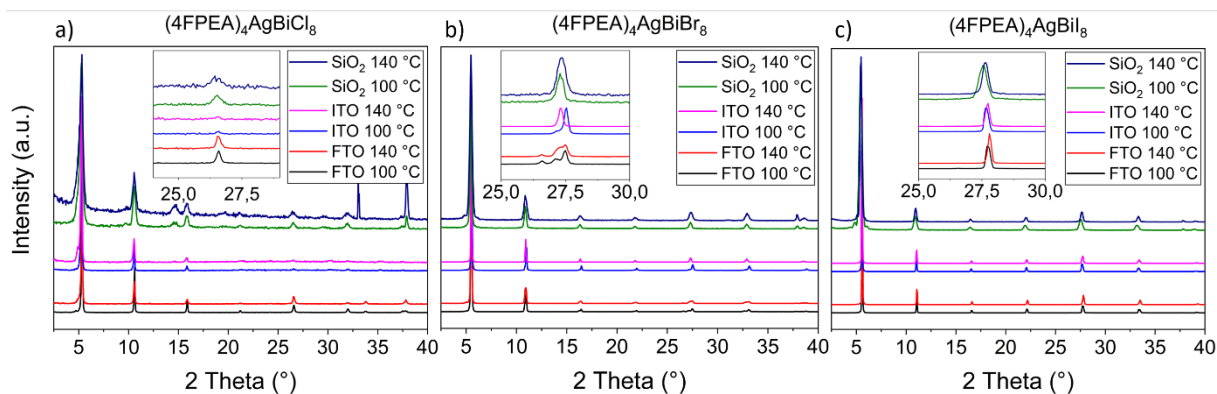


Figure S9: XRD patterns of thin films of a) (4FPEA)₄AgBiCl₈, b) (4FPEA)₄AgBiBr₈ and c) (4FPEA)₄AgBiI₈ on substrates FTO, ITO and SiO₂ from NMP solution with annealing at 100 °C or 140 °C. The different parameters are indicated in the legends, insets show a magnified view of the 005 reflection.

(4FPEA)₄AgBiCl₈: The films of (4FPEA)₄AgBiCl₈ on FTO and ITO exhibit similar patterns, albeit with smaller intensities and slightly worse signal-to-noise ratio (S/N) on ITO. The S/N is further worsened on SiO₂, which can mainly be attributed to the film being thinner compared to the ones on FTO and ITO due to the reduced concentration of the spin coating solution. Additionally, films on SiO₂ show small, additional reflections and the film annealed

at 140 °C shows the distinct reflection of the Si substrate at 33° 2 θ . A broadening of the reflections can be observed for films on SiO₂ compared to the ones on FTO and ITO.

(4FPEA)₄AgBiBr₈: Thin films of (4FPEA)₄AgBiBr₈ follow the same trends, with two differences. Firstly, the crystallinity, i.e. the S/N under consistent scanning conditions, for all three substrates is better than for the chloride films. Secondly, the thin films on FTO display small additional reflections, best observed in the range from 15 to 35° 2 θ . The increased annealing temperature of 140 °C vs. 100 °C for FTO films shows a shift of intensity, increasing the relative intensities of the lower angle reflections, yet the same general reflection positions are seen for both temperatures. This shift is more clearly observed in the thin films on ITO, where for both temperatures distinct, singular reflections are observed. For films annealed at 140 °C the reflections are shifted more clearly towards the lower angle region, while the films annealed at 100 °C have the reflections shifted towards higher angles but also show a remnant of the lower angle reflections (inset of Figure S9 b). The films on SiO₂ substrates display the same large broadening, compared to their respective FTO or ITO analogs. For clarity, a magnification of the reflections from 15 to 35 ° 2 θ with the calculated diffractogram of (4FPEA)₄AgBiBr₈ is given in Figure S10, which shows that the reflection profile is not caused by neighboring reflections, but shows splitting characteristics.

(4FPEA)₄AgBiI₈: Thin films of (4FPEA)₄AgBiI₈ have the highest S/N and hence presumably the highest degree of crystallinity of the three materials. There are no additional reflections and no reflection splitting, as observed in (4FPEA)₄AgBiCl₈ and (4FPEA)₄AgBiBr₈. Interestingly, the influence of the annealing temperature is opposite to that of (4FPEA)₄AgBiBr₈. With higher temperature the reflections shift towards higher angles compared to the diffractograms of samples annealed at 100 °C. This leads to the conclusion that while films of (4FPEA)₄AgBiBr₈ at 140 °C display increased lattice parameters and tensile stress, films of (4FPEA)₄AgBiI₈ show decreased lattice parameters and thus compressive stress. This trend is seen for all three substrates and while again the SiO₂ films show broad reflections, they are also shifted towards higher angles.

S10

Zoom in on the splitting features of $(4\text{FPEA})_4\text{AgBiBr}_8$ thin film diffractograms with the calculated diffractogram from the single crystal structure.

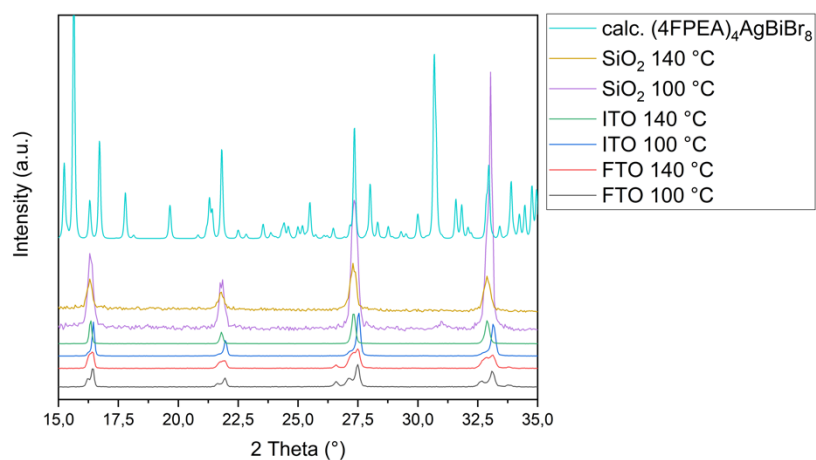


Figure S10: XRD zoom in from $15\text{-}35^\circ$ 2θ of the thin films of $(4\text{FPEA})_4\text{AgBiBr}_8$ on all three substrates FTO, ITO and SiO_2 for both annealing temperatures 100°C and 140°C .

Table S4

Table S4: Profile refinements for thin films of $(4\text{FPEA})_4\text{AgBiBr}_8$ and $(4\text{FPEA})_4\text{AgBiI}_8$ identifying the two phases

	a (Å)	b (Å)	c (Å)	α (°)	β (°)	γ (°)
$(4\text{FPEA})_4\text{AgBiBr}_8$	8.3833	8.1395	32.7693	90	96.120	90
$(4\text{FPEA})_4\text{AgBiBr}_8$ – ITO 100°C	8.3797	8.1441	32.8066	90	96.016	90
$(4\text{FPEA})_4\text{AgBiBr}_8$ – ITO 140°C	8.3407	8.1666	32.9159	90	96.021	90
$(4\text{FPEA})_4\text{AgBiI}_8$	8.6236	8.7470	16.3676	98.973	90.119	90.013
$(4\text{FPEA})_4\text{AgBiI}_8$ – ITO 100°C	8.6938	8.7752	16.3885	98.839	90.587	89.684
$(4\text{FPEA})_4\text{AgBiI}_8$ – ITO 140°C	8.7153	8.8009	16.3610	98.992	91.025	89.778

S11 and S12

The thin film samples have been probed under varying incident angles from 0.04° - 1.00° to evaluate the degree of orientation throughout the complete depths of the films. The penetration depth of the incident X-ray beam can be estimated by using the relation of refractive properties of the material and the incident angle, as shown in equation 1. The index of refraction was calculated in dependence of the X-ray beam energy and the density of the probed material.^[8]

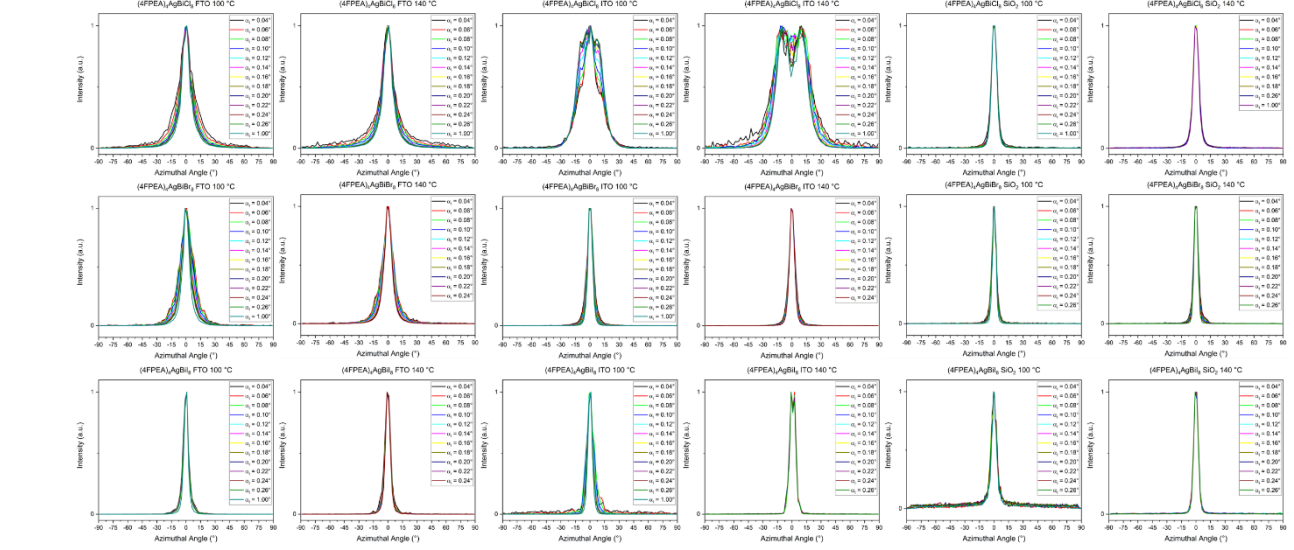


Figure S11: Azimuthal cuts of the 001 reflex for all thin films of $(4FPEA)_4AgBiCl_8$, $(4FPEA)_4AgBiBr_8$ and $(4FPEA)_4AgBiI_8$ on FTO, ITO and SiO_2 annealed at $100^\circ C$ and $140^\circ C$, measured with incident angles from $\alpha_i = 0.04^\circ$ to 1.00° (parameter in the panels).

All three materials have decreasing FWHMs of χ going from FTO to ITO to SiO_2 .

Interestingly, while all samples have their maxima at $\chi = 0^\circ$, corresponding to an exclusively horizontal orientation relative the substrate, $(4FPEA)_4AgBiCl_8$ samples on ITO have a slightly tilted horizontal orientation with peak shouldering for $100^\circ C$ and peak splitting with maxima for $140^\circ C$, both at $\chi = 10^\circ$ and -10° . This small tilting can also be observed in $(4FPEA)_4AgBiI_8$ on ITO at $140^\circ C$, albeit with minimally off-centered maxima at $\chi = 1^\circ$ and -1° . To further probe the degree of orientation, we examined the films at varying incident angles from $\alpha_i = 0.04^\circ$ to 1.00° , to distinguish the surface layers (i.e. several nm) from the complete film depth (i.e. several tens to hundreds nm. The impact of incident angle on penetration depth is further explained in S12).

S12 Equation 1 shows the dependence of the penetration depth Λ on the wavenumber k , the X-ray incident angle α_i , the critical angle α_c and the imaginary part of the index of refraction β .

$$\Lambda = \left[\sqrt{2}k * \sqrt{\sqrt{(\alpha_i^2 - \alpha_c^2)^2 + 4\beta^2} - (\alpha_i^2 - \alpha_c^2)} \right]^{-1} \quad (1)$$

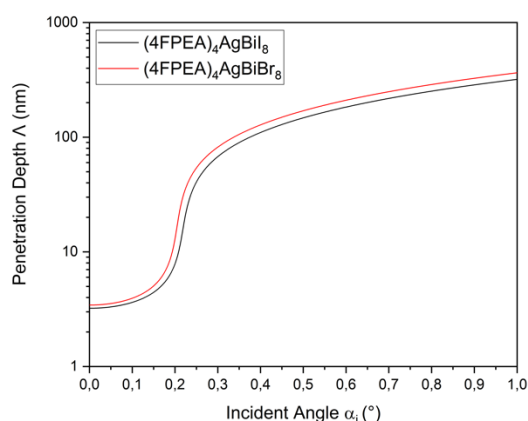


Figure S12: Penetration depth of the X-ray beam under grazing incidence as a function of the incident angle for $(4\text{FPEA})_4\text{AgBiBr}_8$ and $(4\text{FPEA})_4\text{AgBiI}_8$ according to equation (1).

S13

Optical and scanning electron microscope images in Figure S13 demonstrating the effect of the increased annealing temperature on the domain size on thin films of $(4\text{FPEA})_4\text{AgBiI}_8$ a)+b), $(4\text{FPEA})_4\text{AgBiBr}_8$ c)+d) and $(4\text{FPEA})_4\text{AgBiCl}_8$ e)+f).

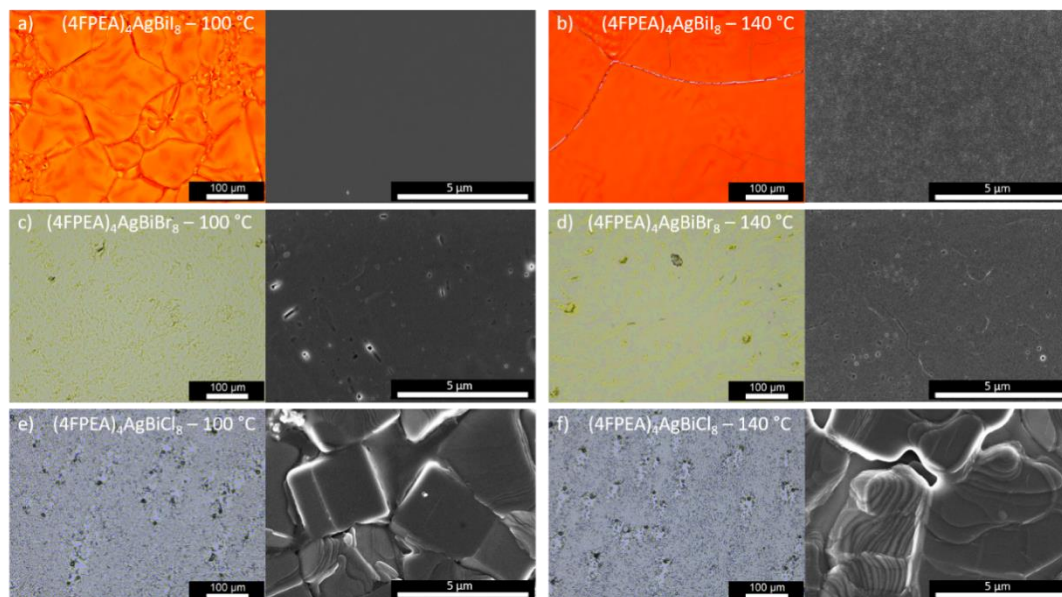


Figure S13: Microscope images of thin films spin coated from NMP solution on ITO of $(4\text{FPEA})_4\text{AgBiI}_8$ annealed at 100 °C a) and 140 °C b), $(4\text{FPEA})_4\text{AgBiBr}_8$ annealed at 100 °C c) and 140 °C d) and $(4\text{FPEA})_4\text{AgBiCl}_8$ annealed at 100 °C e) and 140 °C f).

S14

To confirm the crystal phase of our thin films we indexed 2D images of GIWAXS measurements at a sample detector distance of 155.7865 mm and an incident angle of 0.25 °. Representatively, we measured thin film samples on ITO substrates annealed at 140 °C for a) $(4\text{FPEA})_4\text{AgBiCl}_8$, b) $(4\text{FPEA})_4\text{AgBiI}_8$ and c) $(4\text{FPEA})_4\text{AgBiI}_8$ with the lattice parameters shown in Table S1 and the indexed 2D images shown in Figure S14. Indexing of the GIWAXS data was carried out with the program GIXSGUI.^[9] While the diffraction positions

of (001) planes agree well with the calculated positions, the diffraction positions of planes including a and b lattice parameters exhibit a shift indicating a compressed unit cell in a and b . This agrees with the observed lattice compression between thin films and calculated diffractograms in main text Figure 2.

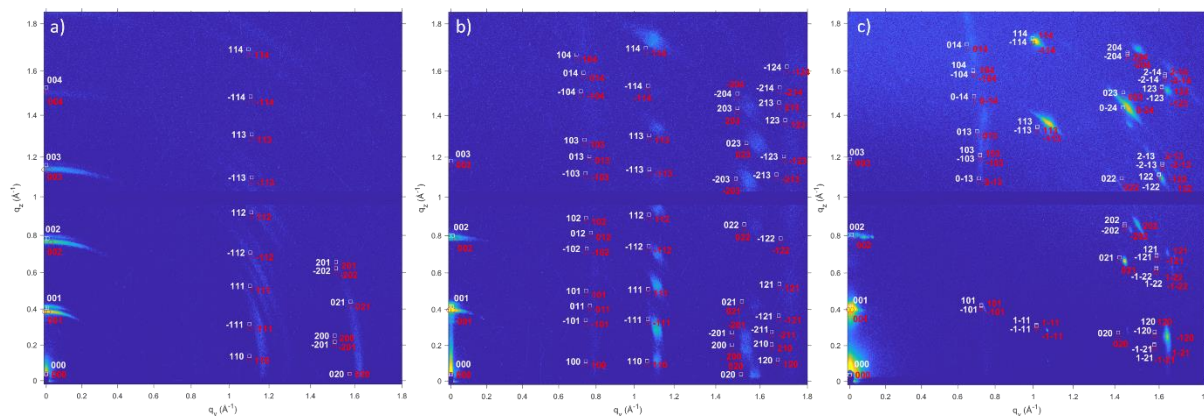


Figure S14: GIWAXS 2D images with indexed diffraction positions for a) $(4\text{FPEA})_4\text{AgBiCl}_8$, b) $(4\text{FPEA})_4\text{AgBiI}_8$ and c) $(4\text{FPEA})_4\text{AgBiI}_8$ thin films on FTO substrates annealed at $140\text{ }^\circ\text{C}$.

S15 and S16

The optimized synthesis parameters for thin films of $(4\text{FPEA})_4\text{AgBiBr}_8$ to yield the same pristine surface morphology as the in the main text shown $(4\text{FPEA})_4\text{AgBiI}_8$ thin film, were different by that the spin coating took place under ambient conditions and the initial spin coating step was at 1000 rpm and the second step was at 6000 rpm.

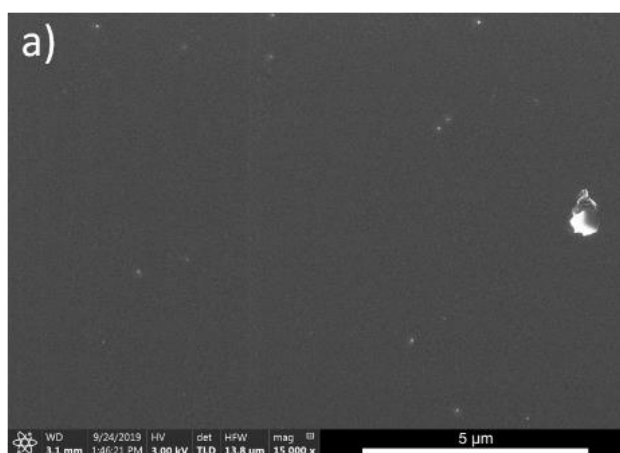


Figure S15: Pristine surface morphology from optimized synthesis parameters for $(4\text{FPEA})_4\text{AgBiBr}_8$ films on FTO.

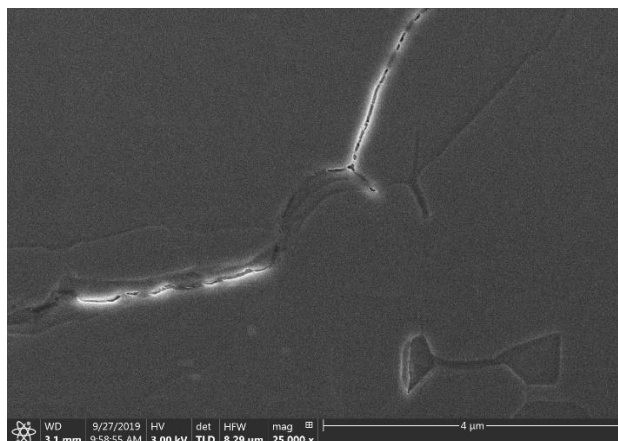


Figure S16: Surface morphology of $(\text{PEA})_4\text{AgBiBr}_8$ thin films on FTO.

S17, S18 and S19

Figure S17 shows the indirect nature of the band gap for $(4\text{FPEA})_4\text{AgBiBr}_8$ and $(4\text{FPEA})_4\text{AgBiI}_8$ if spin-orbit coupling is not considered.

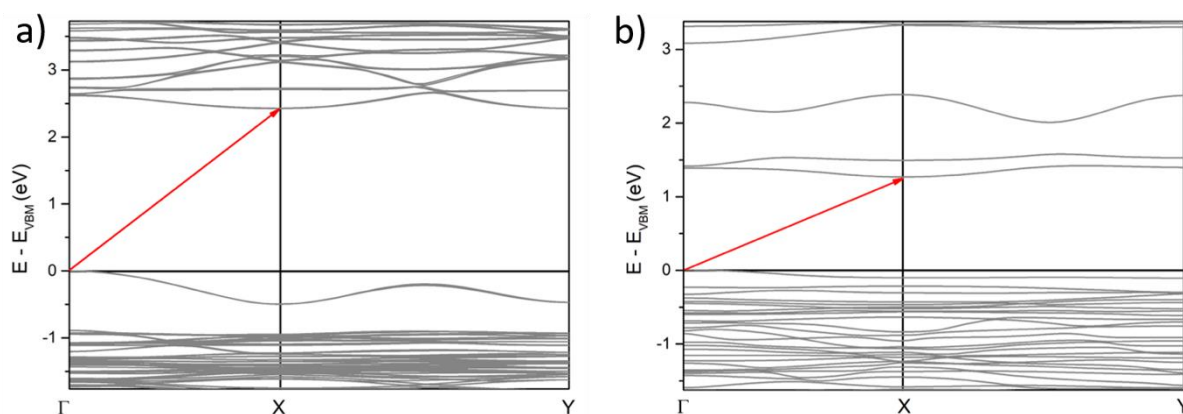


Figure S17: Band structures of a) $(4\text{FPEA})_4\text{AgBiBr}_8$ and b) $(4\text{FPEA})_4\text{AgBiI}_8$ without SOC.

To gather more understanding into the type of quantum well band alignment in these hybrid materials, the partial density of states for organic and inorganic components is depicted in Figure S18.

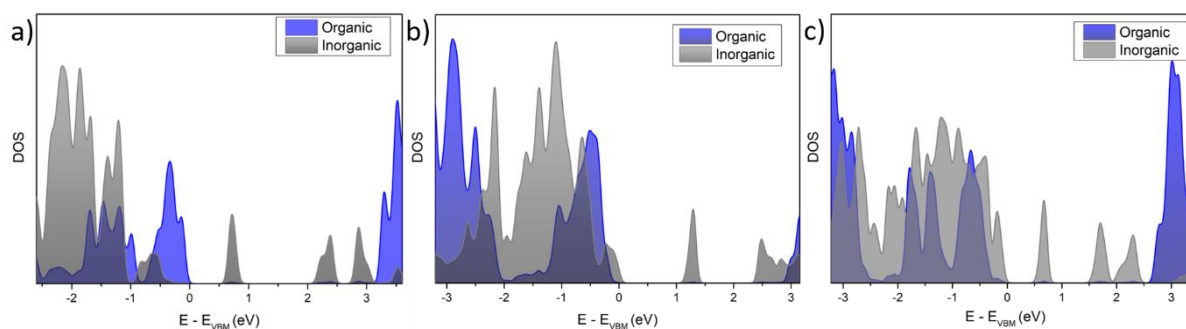


Figure S18: Partial DOS for organic and inorganic components for a) $(4\text{FPEA})_4\text{AgBiCl}_8$, b) $(4\text{FPEA})_4\text{AgBiBr}_8$ and c) $(4\text{FPEA})_4\text{AgBiI}_8$.

To approximate the values for the effective masses at the high symmetry point Γ in the calculated band diagrams for the bromide and iodide compounds, a simple parabolic fit function was employed. The curvature values were used to calculate the effective masses as shown in the following equation:

$$m^* = \hbar^2 \left(\frac{\partial^2 E}{\partial k^2} \right)^{-1}$$

Where $m^*(k)$, \hbar , $E(k)$, and k are the effective mass, reduced Planck's constant, energy, and wave vector, respectively. The obtained values are depicted in Table S5:

Table S5: Effective masses of electrons and holes.

	Bromide	Iodide
Effective masses of electrons [m_e^*/m_0] ($\Gamma - X/\Gamma - Y$)	0.136	0.122
Effective masses of holes [m_h^*/m_0] ($\Gamma - X/\Gamma - Y$)	0.123	0.242

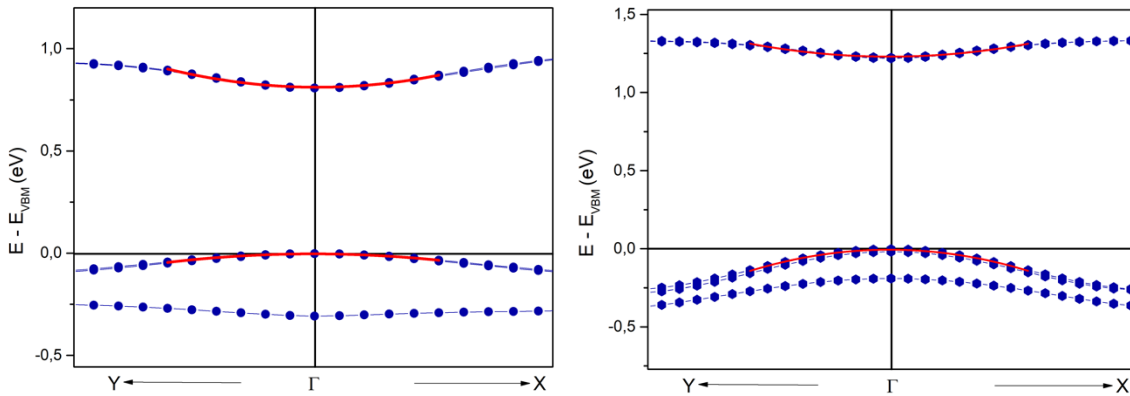


Figure S19: E(k) diagrams for (4FPEA)₄AgBiBr₈ (left) and (4FPEA)₄AgBiI₈ (right).

As expected from the dispersion in the E(k) diagrams, the value for the effective hole mass is much larger for 4FPEAI than for 4FPEABr. The effective electron masses differ by a small amount, also apparent in the band structure plot, with the conduction band being slightly less dispersed for 4FPEABr. We note that the exact prediction of effective mass values requires higher levels of theory, which were not accessible because of the prohibitive system dimensions, but PBE-SOC was also shown to provide satisfactory experimental agreement.^[10]

S20

The theoretical absorption spectra were simulated by calculating frequency-dependent complex dielectric functions as implemented in the Quantum espresso epsilon package according to equation 2.^[11]

$$\alpha(\omega) = \frac{4\pi\omega}{hc} \left[\frac{\sqrt{\text{Re}\epsilon(\omega)^2 + \text{Im}\epsilon(\omega)^2} - \text{Re}\epsilon(\omega)}{2} \right]^{0.5} \quad (2)$$

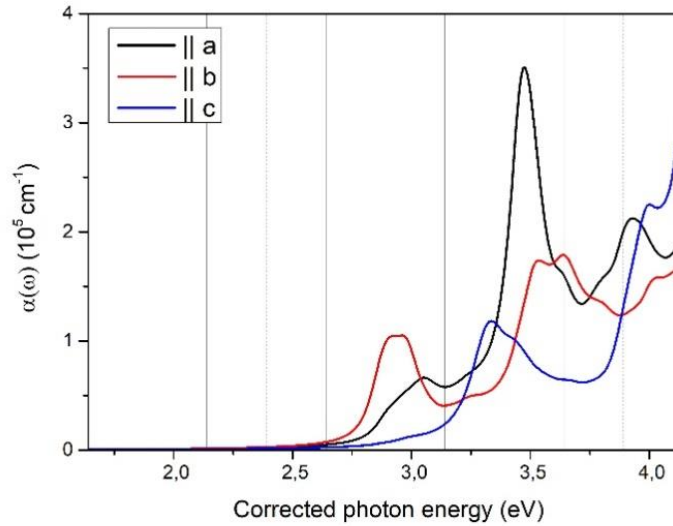


Figure S20: Simulated absorption for $(4\text{FPEA})_4\text{AgBiBr}_8$ from dielectric response employing the random phase approximation excluding excitonic effects and subtracting the experimental absorption edge.

S21

Employed spectral corrections in equation 3, which takes into account the absorption of light reflected from all interfaces, derived by Klahr and Hamann.^[12] Here, A_{corr} represents the corrected absorption, while T_{sub} , T_{sam} , R_{sub} , R_{sam} represent the spectral transmittance and reflectance of the substrate and the coated substrate, respectively.

$$A_{\text{corr}}(\lambda) = -\log \frac{\frac{T_{\text{sam}}(\lambda)}{T_{\text{sub}}(\lambda)}}{1 - \frac{(R_{\text{sam}}(\lambda) - R_{\text{sub}}(\lambda))}{(T_{\text{sub}}(\lambda))^2}} \quad (3)$$

Powder samples were measured as diffuse reflectance spectra with a white standard (BaSO_4) background.

Zoom in on the powder absorption spectra displaying similar features as the thin film absorption spectra:

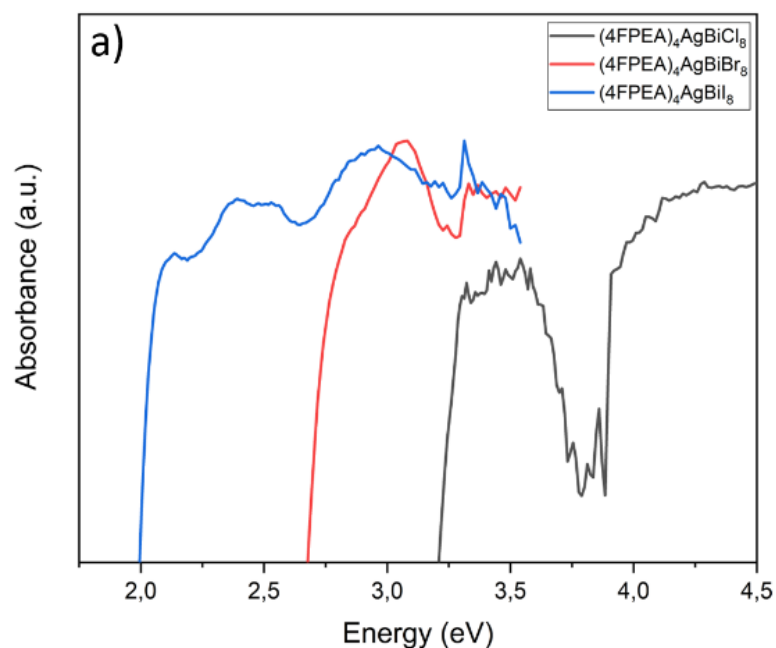


Figure S21: Magnification of the absorption features of powder UV-Vis absorbance data for $(4FPEA)_4AgBiCl_8$, $(4FPEA)_4AgBiBr_8$ and $(4FPEA)_4AgBiI_8$.

S22

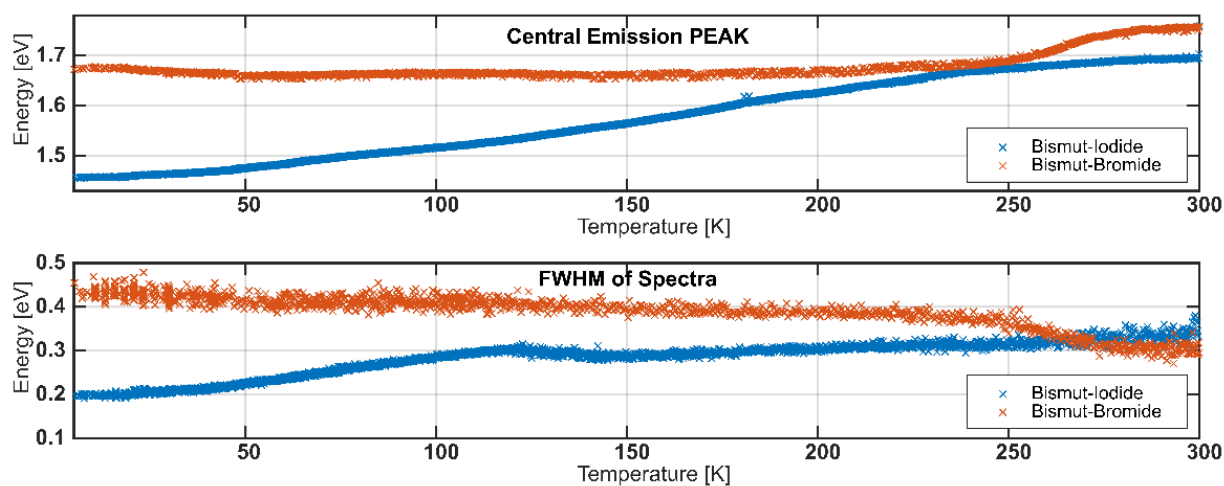


Figure S22: Temperature dependent spectral shift of the central emission peak and FWHM of the PL spectra for $(4FPEA)_4AgBiBr_8$ and $(4FPEA)_4AgBiI_8$.

S23, S24, S25, S26

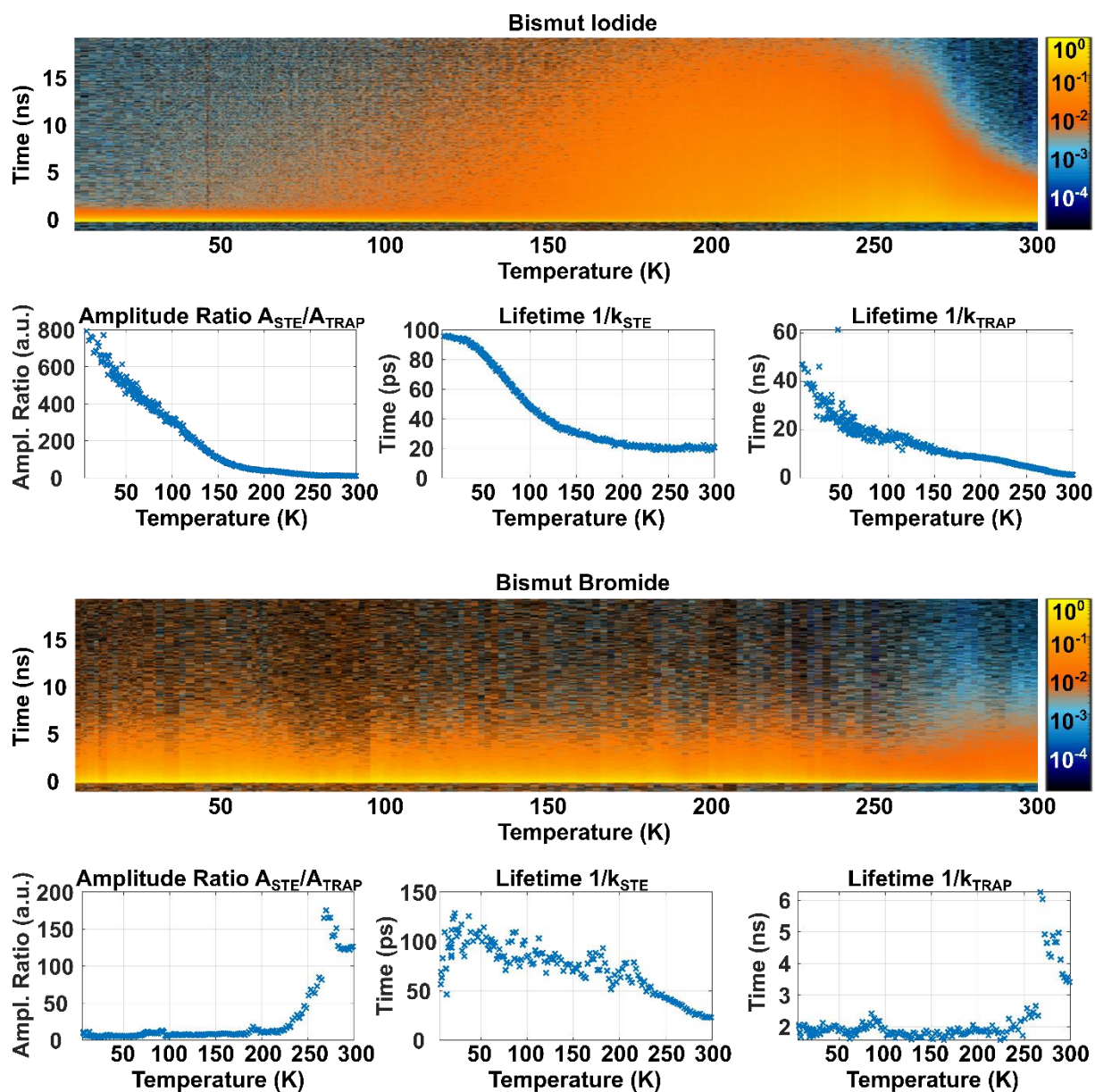


Figure S23: Temperature dependent transients and extracted lifetime plots for the short- and long-lived component from a biexponential fitting for $(4FPEA)_4AgBiBr_8$ and $(4FPEA)_4AgBiI_8$.

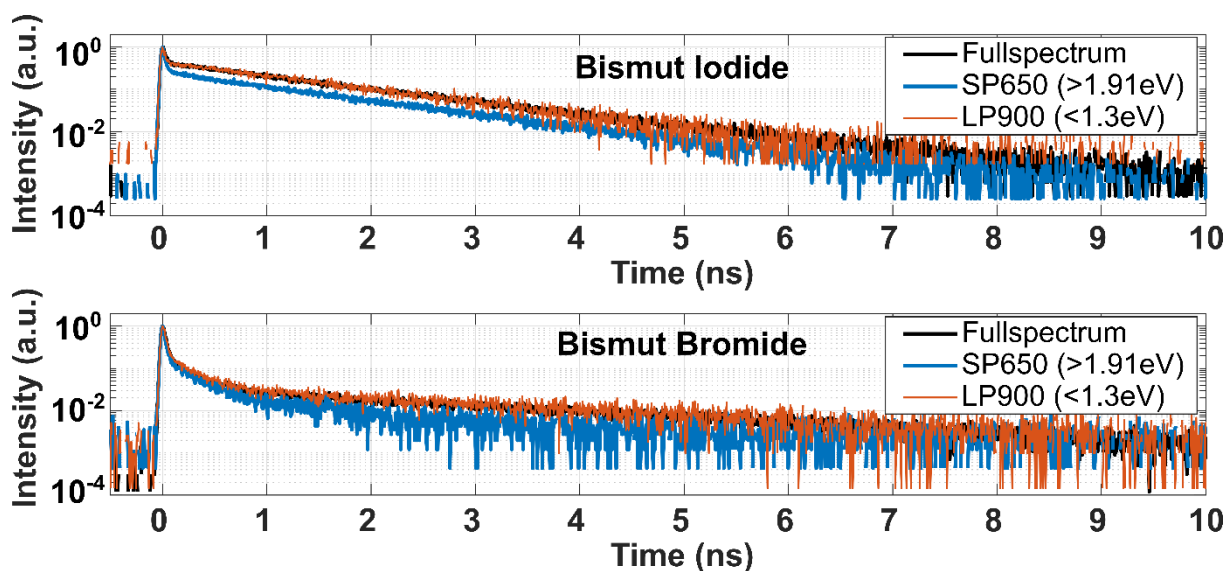


Figure S24: PL transients at room temperature with full spectrum (black), short-pass filter 700/650 nm (blue) and long-pass filter 900 nm (red) for $(4\text{FPEA})_4\text{AgBiBr}_8$ and $(4\text{FPEA})_4\text{AgBiI}_8$.

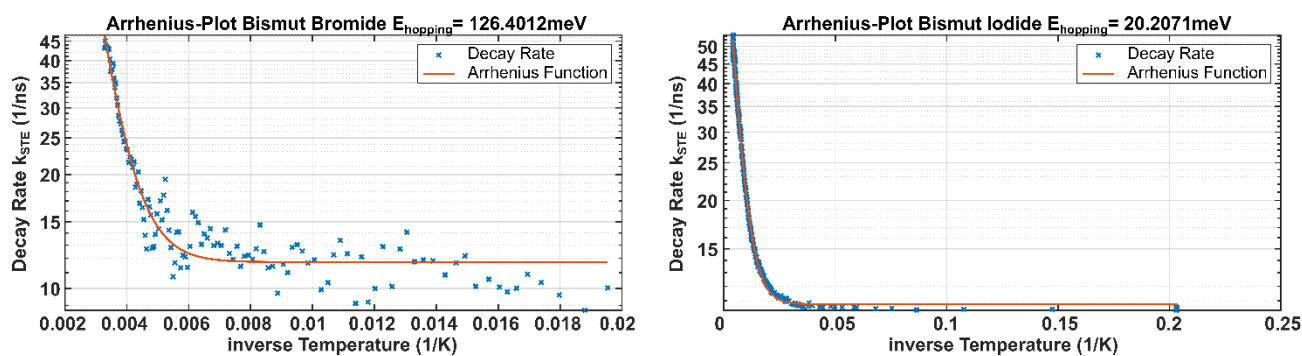


Figure S25: Arrhenius plots to extract the activation energy of the proposed hopping barrier for $(4\text{FPEA})_4\text{AgBiBr}_8$ (left) and $(4\text{FPEA})_4\text{AgBiI}_8$ (right).

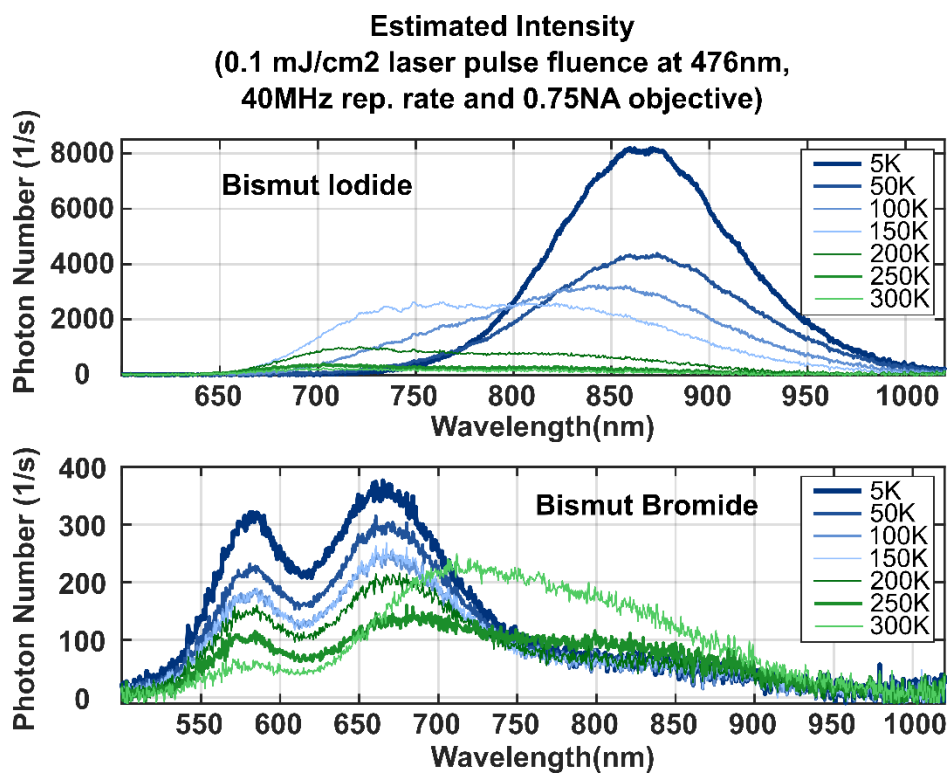


Figure S26a: Estimated intensities of the temperature dependent emission for $(4\text{FPEA})_4\text{AgBiI}_8$ at the top and $(4\text{FPEA})_4\text{AgBiBr}_8$ at the bottom.

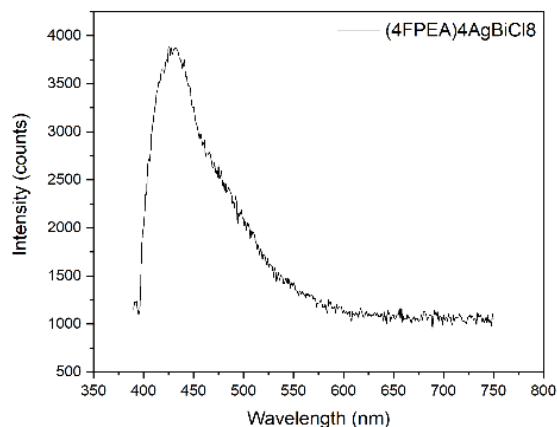


Figure S26b: Room temperature PL spectrum of $(4\text{FPEA})_4\text{AgBiCl}_8$ with excitation wavelength of 375 nm, displaying the same characteristic broad emission as for the bromide and iodide thin films.

S27

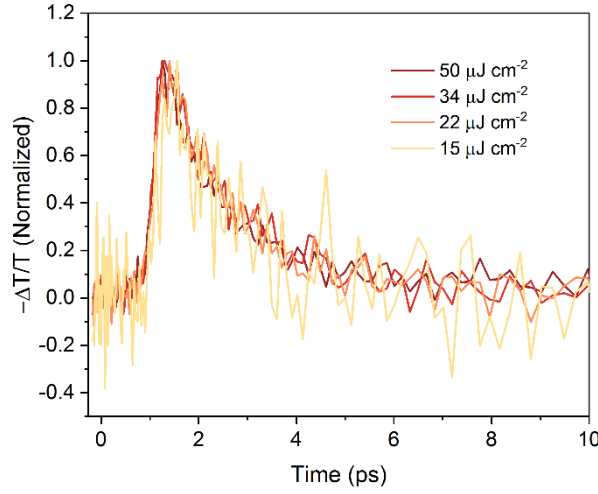


Figure S27: Comparison between normalized fluence-dependent OPTP transients for $(4FPEA)_4AgBiI_8$ after 3.1-eV pulsed excitation. Different coloured lines represent different fluences in the range 15-50 $\mu J cm^{-2}$

S28

Derivation of charge-carrier mobility from OPTP measurements

The charge-carrier mobility was determined using the approach developed by Wehrenfennig et al.^[13] Furthermore, we fitted the OPTP transient with a two-level mobility model developed by Wright et al. and Buizza et al.^[14, 15] In the adopted method, we converted the $\left(\frac{\Delta T}{T}\right)$ traces to a photoconductivity signal $\Delta\sigma$, which is proportional to the charge-carrier mobility μ and to the charge carrier density n via the equation $\Delta\sigma = en\mu$. For our experimental geometry (i.e., transmission geometry for thin film on a z-cut quartz substrate), the sheet photoconductivity can be approximated to

$$\Delta\sigma = -\frac{\epsilon_0 c(n_q + n_v)}{d_{film}} \left(\frac{\Delta T}{T}\right) \quad (S1)$$

where d_{film} is the thickness of the studied thin film and $n_q = 2.13$ and $n_v = 1$ are the refractive indexes of quartz and vacuum, respectively.^[16]

Therefore, in order to derive the charge-carrier mobility from the sheet photoconductivity, the photogenerated carrier number N needs to be determined as

$$N = \phi \frac{E\lambda}{hc} (1 - R_{pump} - T_{pump}) \quad (S2)$$

Where ϕ is the photon-to-charge branching ratio (i.e., the fraction of generated charges per photons absorbed), E is the excitation energy per pulse, $\epsilon = hc/\lambda$ is the energy of a photon with wavelength λ , and R_{pump} and T_{pump} are the reflectance and transmittance of the sample at

the excitation wavelength. This is converted to the photogenerated charge carrier density n_0 by dividing the film thickness d_{film} and the effective overlap area between THz and pump beam A_{eff} .

The resulting effective mobility can be then expressed as:

$$\phi\mu = -\epsilon_0 c(n_q + n_v) \frac{A_{eff} h c}{e E \lambda (1 - R_{pump} - T_{pump})} \left(\frac{\Delta T}{T} \right) \quad (S3)$$

To better capture the photoconductivity dynamics in silver-bismuth halides, Wright and Buizza developed a two-level mobility model, which describes the charge carrier localization process.^[14, 15] In this model, the photoconductivity of the material can be described as the sum photoconductivity for two different states with a definite population and mobility: a delocalized state (n_{del}, μ_{del}) and a localized state (n_{loc}, μ_{loc}) . The resulting photoconductivity can be expressed as $\Delta\sigma = e(n_{del}\mu_{del} + n_{loc}\mu_{loc})$. In the low excitation fluence regime, where the recombination from the localized state is predominantly monomolecular, the carrier population is described by the set of coupled rate equations:

$$\begin{cases} \frac{dn_{del}}{dt} = -k_{loc}n_{del}(t) \\ \frac{dn_{loc}}{dt} = k_{loc}n_{del}(t) - k_1n_{loc}(t) \end{cases} \quad (S4)$$

Here, k_{loc} and k_1 are the localization and monomolecular recombination rates, respectively. As reported in Refs 14 and 15, the resulting $\Delta T/T$ signal can be described as:

$$\frac{\Delta T}{T} = -\frac{en_0 d_{film}}{\epsilon_0 c(n_q + n_v)} \left(\left(\mu_{del} - \frac{\mu_{loc} k_{loc}}{k_{loc} - k_1} \right) e^{-k_{loc}t} + \frac{\mu_{loc} k_{loc}}{k_{loc} - k_1} e^{-k_1 t} \right) \quad (S5)$$

Furthermore, to fit the experimental data reported in Figure 10, we convoluted the resulting decay function with a Gaussian function with broadening $\sigma = 290$ fs (representing the instrumental response function) as described in Reference.^[14]

S29

Although the responsivity of a photodetector gives a measure of the output signal of the detector for a given optical input signal, it does not give any information about the sensitivity

of the device. The sensitivity of the detector can be defined as the minimum detectable optical input power that can be sensed with a signal-to-noise ratio of unity. This power is called the noise-equivalent-power (NEP) of the detector and the detectivity of a detector is the inverse of this noise-equivalent-power. The specific detectivity is denoted D^* and is the detectivity of a photodetector with an area of 1 cm^2 and an electrical bandwidth of 1 Hz , where A is the area of the detector in cm^2 . D^* is expressed in units of $\text{cm}\cdot\text{Hz}^{1/2}\cdot\text{W}^{-1}$.

$$D^* = D\sqrt{A\Delta f} = \sqrt{A\Delta f} \frac{1}{P_{NEP}}$$

S30

Table S6: Summary of related photoconductors.

Active layer		Responsivity (A/W)	Specific Detectivity (Jones)	Reference
2D Sn(II) based perovskites	(PEA) ₂ SnI ₄	16	$1.92 \cdot 10^{11}$	[17]
	graphene/ (PEA) ₂ SnI ₄ /MoS ₂ /graphene	121	$8.09 \cdot 10^9$	[18]
	(PEA) ₂ SnI ₄	329	$2.06 \cdot 10^{11}$	[19]
3D Ag-Bi based double perovskites	Cs ₂ AgBiBr ₆	7.01	$5.66 \cdot 10^{11}$	[20]
	Cs ₂ AgBiBr ₆ / SnO ₂ heterojunctions	0.11	$2.1 \cdot 10^{10}$	[21]
	Cs ₂ AgBiBr ₆	0.14	$3.29 \cdot 10^{12}$	[22]
2D Ag-Bi based double perovskites	(4FPEA) ₄ AgBiBr ₈	0.010	$6 \cdot 10^9$	This work
	(4FPEA) ₄ AgBiI ₈	0.002	$5 \cdot 10^8$	This work
	(R/S-β-MPA) ₄ AgBiI ₈ – microwire array	0.052	$3.9 \cdot 10^{11}$	[23]
	(R/S-β-MPA) ₄ AgBiI ₈ – single crystal	0.000022	$1.2 \cdot 10^7$	[24]

Crystallographic data (4FPEA)₄AgBiBr₈

net formula	C ₃₂ H ₄₄ AgBiBr ₈ F ₄ N ₄
M_r /g mol ⁻¹	1516.84
crystal size/mm	0.050 × 0.050 × 0.020
T /K	297.(2)
radiation	MoK _α
diffractometer	'Bruker D8 Venture TXS'
crystal system	monoclinic
space group	'P 1 2/n 1'
a /Å	8.3833(2)
b /Å	8.1395(2)
c /Å	32.7693(7)
α /°	90
β /°	96.1200(10)
γ /°	90
V /Å ³	2223.30(9)
Z	2
calc. density/g cm ⁻³	2.266
μ /mm ⁻¹	11.626
absorption correction	Multi-Scan
transmission factor range	0.53–0.80
refls. measured	32609
R_{int}	0.0451
mean $\sigma(I)/I$	0.0439
θ range	2.579–29.129
observed refls.	5392
x, y (weighting scheme)	0, 24.9411
hydrogen refinement	mixed
refls in refinement	5973
parameters	233
restraints	0
$R(F_{\text{obs}})$	0.0489
$R_w(F^2)$	0.1302

<i>S</i>	1.239
shift/error _{max}	0.001
max electron density/e Å ⁻³	1.446
min electron density/e Å ⁻³	-1.333

H(C) constrained, H(N) with ideal geometry but the N-H distances have been allowed to be refined.

Crystallographic data (4FPEA)₄AgBiI₈

net formula	C ₃₂ H ₄₄ AgBiF ₄ I ₈ N ₄
<i>Mr/g mol⁻¹</i>	1892.76
crystal size/mm	0.100 × 0.080 × 0.010
<i>T/K</i>	298.(2)
radiation	MoK _α
diffractometer	'Bruker D8 Venture TXS'
crystal system	triclinic
space group	'P -1'
<i>a/Å</i>	8.6236(6)
<i>b/Å</i>	8.7470(5)
<i>c/Å</i>	16.3676(11)
<i>α/°</i>	98.973(2)
<i>β/°</i>	90.119(2)
<i>γ/°</i>	90.013(2)
<i>V/Å³</i>	1219.51(14)
<i>Z</i>	1
calc. density/g cm ⁻³	2.577
<i>μ/mm⁻¹</i>	9.109
absorption correction	Multi-Scan
transmission factor range	0.77–0.91
refls. measured	31455
<i>R_{int}</i>	0.0424
mean <i>σ(I)/I</i>	0.0428
<i>θ</i> range	3.171–30.507

observed refls.	6516
x, y (weighting scheme)	0.0412, 7.1338
hydrogen refinement	mixed
Flack parameter	?
refls in refinement	7455
parameters	241
restraints	0
$R(F_{\text{obs}})$	0.0435
$R_w(F^2)$	0.1040
S	1.037
shift/error _{max}	0.001
max electron density/e \AA^{-3}	2.231
min electron density/e \AA^{-3}	-1.350

References SI

- [1] R. J. Baker, P. E. Colavita, D. M. Murphy, J. A. Platts, J. D. Wallis, *J. Phys. Chem. A* **2012**, *116* (5), 1435-1444.
- [2] F. Schmitz, J. Horn, N. Dengo, A. E. Sedykh, J. Becker, E. Maiworm, P. Belteky, A. Kukovecz, S. Gross, F. Lamberti, K. Muller-Buschbaum, D. Schlettwein, D. Meggiolaro, M. Righetto, T. Gatti, *Chem. of Mater.* **2021**, *33* (12), 4688-4700.
- [3] K. Kikuchi, Y. Takeoka, M. Rikukawa, K. Sanui, *Curr. Appl. Phys.* **2004**, *4* (6), 599-602.
- [4] J. Hu, I. W. H. Oswald, S. J. Stuard, M. M. Nahid, N. Zhou, O. F. Williams, Z. Guo, L. Yan, H. Hu, Z. Chen, X. Xiao, Y. Lin, Z. Yang, J. Huang, A. M. Moran, H. Ade, J. R. Neilson, W. You, *Nat. Commun.* **2019**, *10* (1), 1276.
- [5] M. J. Frisch, G. W. Trucks, H. B. Schlegel, G. E. Scuseria, M. A. Robb, J. R. Cheeseman, G. Scalmani, V. Barone, G. A. Petersson, H. Nakatsuji, X. Li, M. Caricato, A. V. Marenich, J. Bloino, B. G. Janesko, R. Gomperts, B. Mennucci, H. P. Hratchian, J. V. Ortiz, A. F. Izmaylov, J. L. Sonnenberg, Williams, F. Ding, F. Lipparini, F. Egidi, J. Goings, B. Peng, A. Petrone, T. Henderson, D. Ranasinghe, V. G. Zakrzewski, J. Gao, N. Rega, G. Zheng, W. Liang, M. Hada, M. Ehara, K. Toyota, R. Fukuda, J. Hasegawa, M. Ishida, T. Nakajima, Y. Honda, O. Kitao, H. Nakai, T. Vreven, K. Throssell, J. A. Montgomery Jr., J. E.

Peralta, F. Ogliaro, M. J. Bearpark, J. J. Heyd, E. N. Brothers, K. N. Kudin, V. N. Staroverov, T. A. Keith, R. Kobayashi, J. Normand, K. Raghavachari, A. P. Rendell, J. C. Burant, S. S. Iyengar, J. Tomasi, M. Cossi, J. M. Millam, M. Klene, C. Adamo, R. Cammi, J. W. Ochterski, R. L. Martin, K. Morokuma, O. Farkas, J. B. Foresman, D. J. Fox, Gaussian 16 Rev. C.01. Wallingford, CT, **2016**.

- [6] R. J. Baker, P. E. Colavita, D. M. Murphy, J. A. Platts, J. D. Wallis, *J. Phys. Chem. A* **2012**, *116* (5), 1435-1444.
- [7] A. Altomare, C. Cuocci, C. Giacovazzo, A. Moliterni, R. Rizzi, N. Corriero, A. Falcicchio, *J. Appl. Crystal.* **2013**, *46* (4), 1231-1235.
- [8] B. L. Henke, E. M. Gullikson, J. C. Davis, *Atomic data and nuclear data tables* **1993**, *54* (2), 181-342.
- [9] Z. Jiang, *J. Appl. Crystal.* **2015**, *48* (3), 917-926.
- [10] J.-P. Yang, M. Meissner, T. Yamaguchi, X.-Y. Zhang, T. Ueba, L.-W. Cheng, S. Ideta, K. Tanaka, X.-H. Zeng, N. Ueno, S. Kera, *Solar RRL* **2018**, *2* (10), 1800132.
- [11] P. Giannozzi, S. Baroni, N. Bonini, M. Calandra, R. Car, C. Cavazzoni, D. Ceresoli, G. L. Chiarotti, M. Cococcioni, I. Dabo, *J. Phys. Cond. Matter* **2009**, *21* (39), 395502.
- [12] B. M. Klahr, T. W. Hamann, *J. Phys. Chem. C* **2011**, *115* (16), 8393-8399.
- [13] C. Wehrenfennig, G. E. Eperon, M. B. Johnston, H. J. Snaith, L. M. Herz, *Adv. Mater.* **2014**, *26*, (10), 1584-1589.
- [14] L. R. V. Buizza, A. D. Wright, G. Longo, H. C. Sansom, C. Q. Xia, M. J. Rosseinsky, M. B. Johnston, H. J. Snaith, L. M. Herz, *ACS Energy Lett.* **2021**, *6*, (5), 1729-1739.
- [15] A. D. Wright, L. R. V. Buizza, K. J. Savill, G. Longo, H. J. Snaith, M. B. Johnston, L. M. Herz, *J. Phys. Chem. Lett.* **2021**, *12*, (13), 3352-3360.
- [16] H. J. Joyce, J. L. Boland, C. L. Davies, S. A. Baig, M. B. J. S. S. Johnston, *Techn.* **2016**, *31*, (10), 103003.
- [17] L. Qian, Y. Sun, M. Wu, C. Li, D. Xie, L. Ding, G. Shi, *Nanoscale* **2018**, *10* (15), 6837-6843.
- [18] C. Fang, H. Wang, Z. Shen, H. Shen, S. Wang, J. Ma, J. Wang, H. Luo, D. Li, *ACS Appl. Mater. Interfaces* **2019**, *11* (8), 8419-8427.
- [19] L. Qian, Y. Sun, M. Sun, Z. Fang, L. Li, D. Xie, C. Li, L. Ding, *J. Mater. Chem. C* **2019**, *7* (18), 5353-5358.
- [20] L.-Z. Lei, Z.-F. Shi, Y. Li, Z.-Z. Ma, F. Zhang, T.-T. Xu, Y.-T. Tian, D. Wu, X.-J. Li, G.-T. Du, *J. Mater. Chem. C* **2018**, *6* (30), 7982-7988.

- [21] C. Wu, B. Du, W. Luo, Y. Liu, T. Li, D. Wang, X. Guo, H. Ting, Z. Fang, S. Wang, Z. Chen, Y. Chen, L. Xiao, *Adv. Opt. Mater.* **2018**, *6* (22).
- [22] J. Yang, C. Bao, W. Ning, B. Wu, F. Ji, Z. Yan, Y. Tao, J. M. Liu, T. C. Sum, S. Bai, J. Wang, W. Huang, W. Zhang, F. Gao, *Adv. Opt. Mater.* **2019**.
- [23] Y. Zhao, M. Dong, J. Feng, J. Zhao, Y. Guo, Y. Fu, H. Gao, J. Yang, L. Jiang, Y. Wu, *Adv. Opt. Mater.* **2021**.
- [24] D. Li, X. Liu, W. Wu, Y. Peng, S. Zhao, L. Li, M. Hong, J. Luo, *Angew. Chem. Int. Ed. Engl.* **2021**, *60* (15), 8415-8418.